Strain Hardening in Graphene Foams under Shear

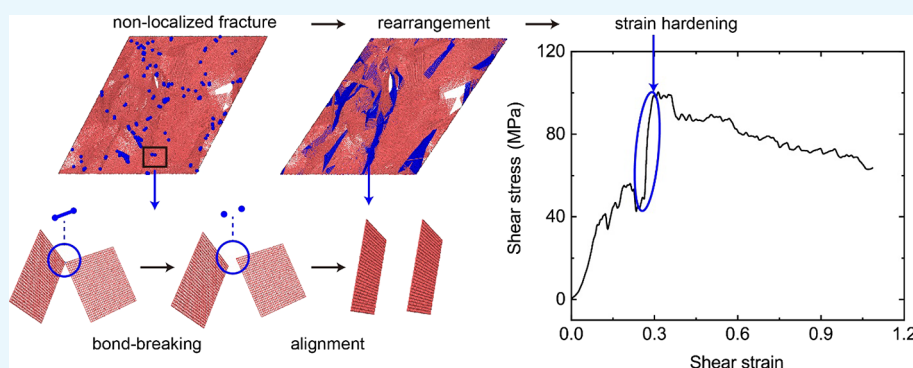Tian Yang, Chao Wang,* and Zuobing Wu*

ACCESS | Metrics & More | Article Recommendations | Supporting Information

ABSTRACT: Strain hardening is an important issue for the design and application of materials. The strain hardening of graphene foams has been widely observed but poorly understood. Here, by adopting the coarse-grained molecular dynamics method, we systematically investigated the microscopic mechanism and influencing factors of strain hardening and related mechanical properties of graphene foams under shear loading. We found that the strain hardening is induced by cumulative nonlocalized bond-breakings and rearrangements of microstructures. Furthermore, it can be effectively tuned by the number of graphene layers and cross-link densities, i.e., the strain hardening would emerge at a smaller shear strain for the graphene foams with thicker sheets and/or more cross-links. In addition, the shear stiffness G of graphene foams increases linearly with the cross-link density and exponentially with the number of graphene layers n by $G \sim n^{1.95}$. These findings not only improve our understanding of the promising bulk materials but also pave the way for optimizing structural design in wide applications based on their mechanical properties.

1. INTRODUCTION

As a new kind of porous bulk assembly of graphene sheets, graphene foams (GrFs) have a series of excellent mechanical[1−3] and physical[4,5] properties. It is reported that they have potential applications in a broad range of fields including energy storage,[6,7] environment purification,[8,9] flexible electronics,[10] and advanced composites.[11]

Both macroscopic mechanical responses and related microstructural evolutions of GrFs under uniaxial compression,[2,12−16] tension,[14−18] and shearing[19,20] have been studied by experiments and simulations due to their basic importance to practical applications. All GrFs in uniaxial compression exhibit a rubber-like response with the typical three periods in the stress−strain curves, i.e., the initial linear elastic stage successively followed by a yielding stage and a final densification one; they show a multipeak stress−strain response under uniaxial tension[17] due to the sheet alignment and intermittent bond-breakings of graphene sheets and cross-links.[18] A similar mechanical response of GrFs has been observed under shear loading using the coarse-grained simulation.[19]

Interestingly, no matter what kind of external load is adopted, the strain hardening that the stress increases with strain after the yield plateau can be identified. It has been well-understood for the strain hardening of GrFs in uniaxial compression as it definitely emerges in the last densification stage due to the rotating and folding of graphene sheets in the direction of compression.[21] Compared to the well-understood densification-induced strain hardening in compression, the strain hardening behavior in the uniaxial tension[15−17] and shearing[19,20] of GrFs remains elusive. On the one hand, some GrF systems[17,19] have obvious single and even multiple hardening behaviors in the loading process, while others[15,16,20] have relatively weak hardening behavior; on the other hand, the critical strain to enter the strain hardening stage varies in different GrFs.

The underlying mechanisms of strain hardening of GrFs should be much different from those of metals and polymers. For metals, the strain hardening is mainly induced by increasing the dislocation density or the lattice resistance
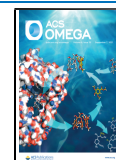
against dislocation sliding by alloying and refining grain size as studied in ref 22; for polymers,[23] the strain hardening is attributed to the stretching and development of the long-range orientation of the entangled polymer network.

The possible factors influencing the strain hardening of GrFs include the density of the foam system, the size and thickness of graphene sheets, and the content of intersheet cross-links. More importantly, some chemical bonds in graphene sheets and cross-links between neighbor sheets would definitely break in both tension and shearing, which would influence the microstructural evolution as well as hardening behaviors. It is difficult to accurately monitor and modulate these factors by existing experimental techniques to study their effect on the hardening of GrFs. Hence, the simulation method is an effective candidate. Actually, the simulation methods of all-atomic molecular dynamics (AAMD) and coarse-grained molecular dynamics (CGMD) have been successfully adopted to study a series of mechanical issues of GrFs. By AAMD, Baimova et al.[20] investigated the mechanical responses of GrFs under hydrostatic pressure and shear strain. Qin et al.[15] showed that GrFs have an exceptionally high ultimate tensile strength 10 times as strong as mild steel but with a relatively low density of 4.6% that of mild steel by combining AAMD simulations and experiments based on 3D printed models. Zhang et al.[24] created a GrF with a specific compressive strength of 9.79 GPa cm^3 g^{-1}, a value that surpasses those of nearly all existing structural materials, and unveiled that the beneficial mechanical properties are enabled by the local deformation of 1 nm curled graphene fragments, the interactions among neighboring fragments, and the presence of covalent carbon−carbon bonds by adopting AAMD simulations. Patil et al.[16,25] studied the fracture behaviors of GrFs using AAMD and found that the fracture toughness shows a power-law dependence on the density with the exponent estimated to be 1.41 ± 0.04; they also studied the shockwave response of GrFs of a wide range of densities from 149 to 679 kg/m^3 and obtained a linear relationship between the shock velocity and the particle velocity. On the basis of CGMD, Wang et al. and Pan et al. systematically investigated the micromechanism and basic characteristics of elasticity of GrFs under compression and tension,[14] uniaxial super-compression, and recovery behavior of GrFs with a hole-flake network.[13] They also unveiled the mesoscopic physical mechanism of a multipeak stress−strain relationship, the ductile fracture mode near the plane 45° from the loading direction under tension,[18] and a rubber-like behavior and a near-zero Poisson's ratio under compression,[21] which are significant characteristics of GrFs observed in experiments.[17] Xia et al.[19] reported that a critical temperature can tune GrFs to be either fluid-like or glassy-like by using CGMD.

In the present study, we apply CGMD to investigate the deformation behaviors and fracture modes of GrFs. A two-dimensional (2D) coarse-grained graphene model developed by Cranford and Buehler[26] is expanded into three-dimensional (3D) to evaluate the mechanical performance of the graphene assembly under shear loading. The rest of this article is organized as follows: First, the 3D GrF model is established by assembling 2D graphene sheets with intersheet cross-links. On this basis, significant strain hardening after yielding a plateau is reproduced, and then, two physical mechanisms leading to the strain hardening are elucidated, including the nonlocalized fracture propagation and the rearrangement of geometry and stress caused by bond-breakings and external loading. Then,

the effect of the configuration parameters, including the number of graphene layers and cross-link densities, on the mechanical properties of GrFs under shear loading is revealed. Finally, the conclusions are given at the end of the paper. These conclusions could not only help deepen the understanding of graphene-based foam materials but also provide insights into the analogous 3D assemblies of ample 2D atomic crystals such as h-BN and MoS$_2$ among others.[27,28]

2. METHODS

2.1. Coarse-Grained Molecular Dynamics. In the coarse-grained (CG) models, groups of atoms are clustered into beads that interact through effective force fields, allowing the mesoscale physical processes to be simulated while retaining the microscale details in a cost-effective manner. The force-field potentials of the CG model adopted in our simulation include bond energy $E_{bond} = k_T(r - r_0)^2/2$, angle energy $E_{angle} = k_B(\theta - \theta_0)^2/2$, and pairwise van der Waals (vdW) interaction $E_{vdW} = 4\varepsilon((\sigma/r)^{12} - (\sigma/r)^6)$, where k_T, r, r_0, k_B, θ, θ_0, ε, and σ are the tensile stiffness, the current bond length, the equilibrium bond length, the bend stiffness, the angle of the triplet, the angle of the equilibrium triplet, the energy well depth, and the zero-energy distance, respectively. All these parameters are taken from full atomistic calculations based on the conservation of potential energy.[26]

In practical preparation, the number of graphene layers can be tuned from 1 to 10 layers in integer intervals,[29] from which the 5-layer GrF is selected in the paper as a representative to illustrate the physical mechanism of strain hardening. The effect of the number of graphene layers is discussed in detail in Section 3.5. The parameters of the main force field in the 5-layer GrF are shown in Table 1, and those in GrFs of different graphene layers can be found in Table S1 in the Supporting Information.

Table 1. The Parameters of the Main Force Field in the 5-Layer GrF

interactions	parameters	values
bond	equilibrium bond distance r_0 (Å)	25
	tensile stiffness k_T (kcal mol^{-1} Å^{-2})	2325
angle	bend stiffness k_B (kcal/mol) ($\theta_0 = 90°$)	84,350
	bend stiffness k_B (kcal/mol) ($\theta_0 = 180°$)	185,601
vdW	Lennard-Jones parameter ε (kcal/mol)	473.0
	Lennard-Jones parameter σ (Å)	15.20
	Lennard-Jones cutoff radius (Å)	30

2.2. Fabrication of Numerical Samples. One of the most common methods in the laboratory to prepare GrFs is the assembly method,[30] which is mainly realized by preparing suspensions of graphene sheets at first and then using suitable methods such as adding cross-link agents to assemble uniformly distributed graphene sheets to 3D porous foam. Analogous to the above assembly method, the coarse-grained model of GrFs is established here and used for subsequent research on mechanical response under shear loading, as shown in Figure 1. As the building block, the coarse-grained model of graphene sheets proposed by Cranford and Buehler[26] is adopted in this paper, in which groups of atoms in the all-atom model are simplified to a coarse grain with an equilibrium bond length of 2.5 nm based on the equivalence of potential energy. Figure 1a-i shows the coarse-grained graphene sheet with a size of 72.5 nm × 72.5 nm. In addition, the fracture of
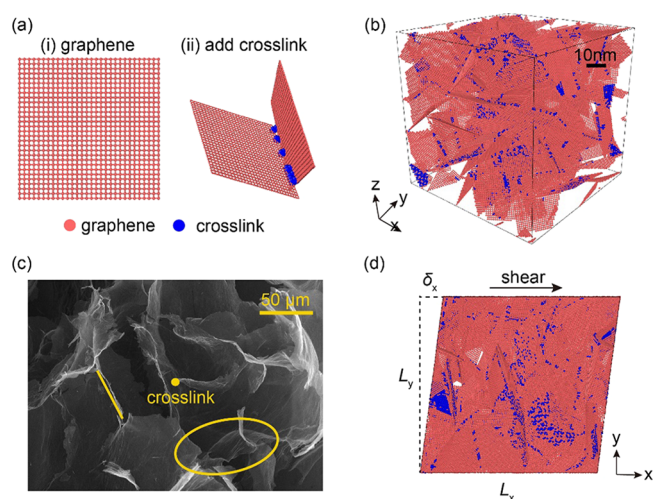
Figure 1. Numerical model of the GrF. (a-i) Building block of a piece of a graphene sheet and (a-ii) cross-links between graphene sheets. (b) 5-layer GrF with cross-links. (c) Scanning electron microscope image of GrF and its cross-link structures. (d) Schematic diagram of shear loading.

graphene is considered in this study, and the fracture strain of chemical bonds is taken to be 12% based on abundant experimental and theoretical research.[31,32]

In numerous experiments and applications, building cross-links among individual graphene sheets has become a widespread functionalization technique used in 3D graphene architectures[33] due to the significant improvement in the properties of GrFs.[34,35] Here, we focus on the mechanical performance of GrFs with intersheet cross-links. The covalent bond model of cross-links with the same force-field parameters of inner-sheet bonds is adopted here to simulate the strong connecting effect in the actual samples caused by either physical cohesion or chemical treatment,[36] as shown by blue points in Figure 1a-ii.

According to the equilibrium bond length (2.5 nm) and fracture strain (12%) of graphene sheets, the distance between the particle pairs of different graphene sheets to decide if cross-links can be generated is set to be 2.2−2.8 nm. When the distance is larger than 2.8 nm, the chemical bonds in the model hardly exist, while the structure will undergo large disturbance in the subsequent geometric optimization when the distance is smaller than 2.2 nm since chemical bonds tend to recover the equilibrium bond length. The total number of cross-links satisfying the above distance requirement is the maximum
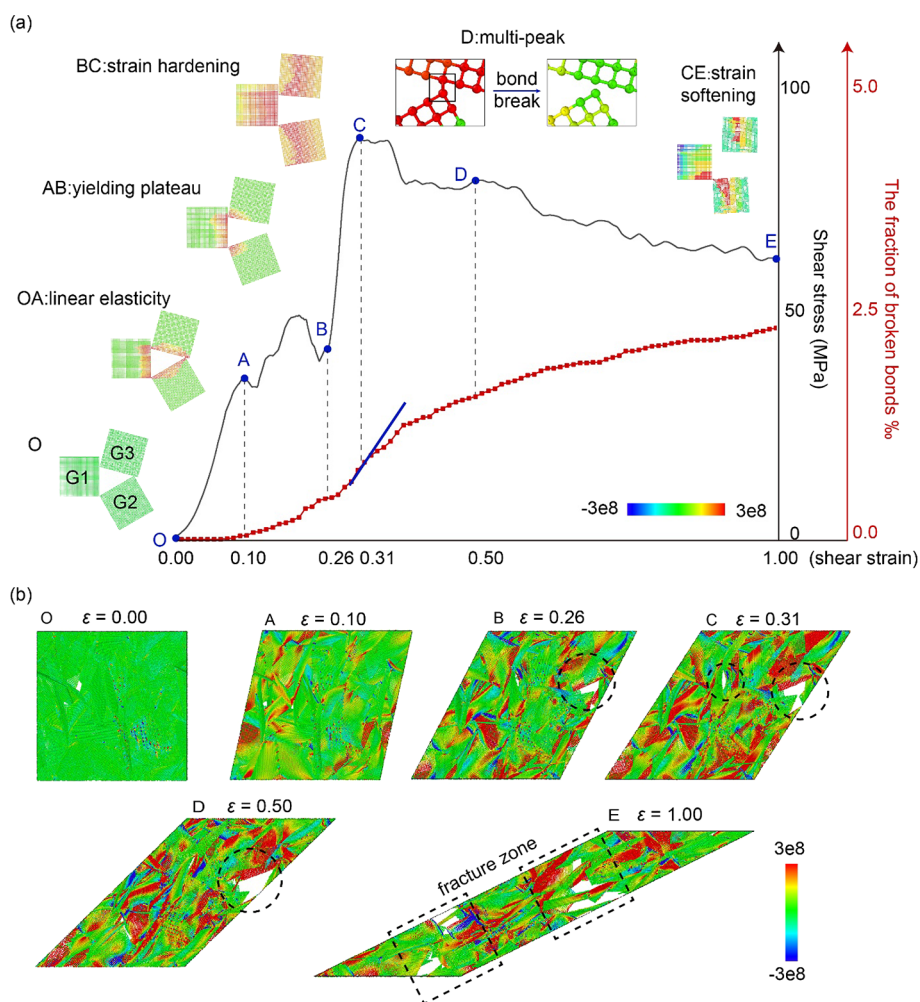

Figure 2. Strain hardening phenomenon in GrFs. (a) Variation of shear stress τ_{xy} and the fraction of broken bonds f_{broken} with shear strain, illustrated by the microstructural evolution of the representative load-bearing unit. (b) Distribution and evolution of stress component τ_{xy} under shear loading.

number of cross-links N_{max} (10,539 in all our simulations), from which the current content of cross-links N_{cur} can be tuned by randomly selecting a specified number of cross-links. Thus, the relative cross-link density ρ is defined as the current number of cross-links N_{cur} divided by the maximum number of cross-links N_{max} in the model. The greater the cross-link density, the better the connectivity in GrFs is. The effect of cross-link densities on mechanical properties is discussed in Section 3.5.

The mesoscopic model of the 5-layer GrF is shown in Figure 1b, where a representative volume element of 235.7 nm × 219.7 nm × 215.8 nm is assembled by 100 identical graphene sheets with a relative cross-link density of 0.47 (corresponding to ~4.5 × 10⁵ cross-links per cubic micrometer). The total energy curves during the equilibrium processes are shown in Figure S1 in the Supporting Information, indicating the realization of energy minimization and geometric optimization. After energy minimization of the system, a stable GrF with cross-links is obtained with a mass density of 39−380 mg/cm³ for 1−10 layers, within the density range of the GrF samples prepared in experiments.[3,33,37] The sample of GrF prepared by an assembly method in the experiments is characterized using a scanning electron microscope, as shown in Figure 1c, in which graphene sheets are disorderly placed and connected by intersheet cross-links in forms of points, lines, and faces. In conclusion, the numerical model is qualitatively consistent with the random network topology, cross-link structure, and material density of the experimental samples, which verifies the rationality of the numerical model.

Simple shear loading is applied to the fully equilibrated model using the deformation-controlled method by varying the tilt factor of the simulation box in the xy plane (Figure 1d). The bottom end of the model is fixed, and the upper surface is stretched at a constant speed of v. The shear strain is defined as $\varepsilon = \delta_x/2L_y$, where δ_x and L_y are the displacement along the x-axis and the dimension of the simulation box along the y-axis, respectively. The enforced strain rate is 2.20×10^6 s⁻¹ with a time step of 10 fs, making the GrF deform from a shear strain of 0.00 to 1.00. The NVT (constant number of atoms, constant volume, and constant temperature) and the Nosé/Hoover temperature thermostat are used to update the positions and velocities of atoms at each time step, and the stress response is calculated based on the virial stress formulation.[38] See more details about the virial stress in Section 2 in the Supporting Information.

To ensure the reliability of results, for each influencing factor, e.g., cross-link density, three numerical samples with different initial microstructures are used to conduct simulations. All the simulations are performed in a large-scale atomic/molecular massively parallel simulator (LAMMPS).[39] The results are visualized based on the Open Visualization Tool (OVITO).[40]

3. RESULTS AND DISCUSSION

3.1. The Strain Hardening Phenomenon.
The mechanical response of the 5-layer GrF is shown in Figure 2. The fracture state of GrFs can be quantitatively characterized by the fraction of broken bonds f_{broken}, which is defined as the current number of broken bonds divided by the total number of chemical bonds in the initial materials. Figure 2a shows the synchronous change laws of shear stress τ_{xy} and f_{broken} with shear strain under external shear loading.

In order to fully reflect the effect of graphene sheets and cross-links and to consider the dynamic evolution of bond-breakings, three graphene sheets G1, G2, and G3 connected by cross-links are used as representative load-bearing units (RLU) to analyze the stress distribution and fracture propagation at different loading periods from the perspective of micro-structures, as shown in the illustrations in Figure 2a. Figure 2b shows the distribution and evolution of stress component τ_{xy} in GrFs of 5-layer graphene sheets under shear loading, and those in GrFs of other layers can be found in Figure S2 in the Supporting Information.

According to the stress−strain curve, the material undergoes four stages under shear loading, including the linear elastic stage OA ($0.00 < \varepsilon < 0.12$), the yield stage AB ($0.12 \leq \varepsilon < 0.26$), the strain hardening stage BC ($0.26 \leq \varepsilon < 0.31$), and the strain softening stage CE ($0.31 \leq \varepsilon < 1.10$). At the beginning of the loading (point O, $\varepsilon = 0.00$), the structure is in the stable state after energy minimization. The value of shear stress is 0, and there is no stress concentration in the RLU. For the whole structure in Figure 2b, there is almost no stress concentration but only a few weak stress concentration areas around some cross-links. The shear stress in the RLU increases linearly in stage OA, as featured by the enlarging and reddening stress concentration areas around the cross-links. According to the curve of f_{broken}, the number of broken bonds keeps to be 0 during this stage, which indicates that no chemical bonds have reached their load-bearing limits yet.

When the shear strain is 0.10 (point A on the stress−strain curve), the cross-link between G2 and G3 in the RLU reaches the load-bearing limit and breaks, and then, the stress concentration near this bond-breaking position is eliminated. Meanwhile, the stress−strain curve enters the yield stage AB during which the value of shear stress changes little. Combined with the change of f_{broken}, it is clear that the emergence of broken bonds directly leads to the yield stage of the GrF. The distribution of shear stress at point A in Figure 2b shows that the stress concentration areas in the GrF increase significantly compared with the initial stress state. Further observation reveals that stress concentration still distributes near cross-links, and connected graphene sheets participate in the formation of the force chains,[41] which is consistent with the analysis of microstructures. Ma and Chen[42] reported that intersheet cross-links can effectively strengthen the mechanical properties of GrFs like improving the tension strength or tension stiffness since cross-links can connect graphene sheets and thus enhance the load-bearing capacity. This cross-link effect is totally consistent with the above structural analysis.

In the porous GrFs, the stress state is directly affected by the macro cumulative competition of two parts, including the stress reduction part caused by bond-breakings and stress rearrangement triggered by external loading. These two factors are not completely independent. Instead, bond-breaking and stress redistribution are often mutually causal, given that bond-breaking will definitely lead to the release of accumulated energy, inevitably causing stress rearrangement, and the stress increase due to the stress rearrangement may promote the chemical bonds to reach their load-bearing limits and finally break.

During the yield stage, the stress reduction caused by bond-breakings plays a leading role. Although only 82 bonds break across the whole structure, accounting for only 0.46‰ of all chemical bonds, these broken bonds are dispersed globally rather than locally, resulting in as many as 56 sheets of

graphene with directly rearranged geometry and stress. Only these directly involved graphene sheets account for 56% of all graphene sheets, and other graphene sheets are indirectly affected by bond-breakings through the interaction among graphene sheets. Due to the nonlocalized distribution of these broken bonds, the value of shear stress is relatively stable and oscillates around 50 MPa in the AB stage, although the external loading is persistent.

The degree of freedom at the original connection is increased because of bond-breakings. In the RLU, the relative position of graphene sheets changes and the shear stress increases under the continuous external loading after bond-breakings. Graphene sheets tend to align to the loading direction, releasing the load-bearing potential of in-plane high-strength characteristic, so stress increases after the instantaneous reduction caused by bond-breakings. From the perspective of microstructural evolution, bond-breaking can lead to the rearrangement of geometry and stress of graphene sheets. On the whole GrF scale, nonlocalized bond-breakings result in the rearrangement of geometry and stress of many graphene sheets, causing GrF's load-bearing ability increases. When this part of cumulative stress increase is greater than the part of stress decrease caused by bond-breakings, the material enters the strain hardening stage BC.

In stage BC, the sharp rise of stress leads to the massive appearance of new broken bonds. According to the curve of f_{broken}, the increase rate of broken bonds featured by the tangent slope of the curve is the fastest in the whole loading process, as shown by the blue line. Seen from Figure 2b, after the bond-breakings and resultant rearrangement of geometry and stress in the yield stage, the stress concentration areas at the beginning of the strain hardening stage (point B, $\varepsilon = 0.26$) increase obviously compared to the stress state at point A, and these areas are distributed all over the GrF rather than in certain local positions. Moreover, due to the slide of graphene sheets under shear loading, holes begin to appear in the structure, as shown by the black dashed circle. In the strain hardening stage, the stress increase caused by stress rearrangement keeps playing a leading role, and the GrF reaches the maximum load-bearing capacity of 98 MPa when the shear strain ε is 0.31. As shown from Figure 2b, the distribution of stress concentration at point C is significantly wider than that at point B and is basically uniform across the structure. The hole appearing at point B expands, and there are new holes developed.

Bond-breakings increase continuously as seen from the curve of f_{broken}, and then, the material undergoes the strain softening stage CE. In this process, the stress decreases as a result of the everlasting bond-breakings. However, the stress curve does not drop monotonously but has some multipeaks like point D. As shown in the RLU at point D, bond-breakings lead to the instantaneous drop of stress followed by the rearrangement of stress under shear loading, so the temporary peak D happens when the stress increase part caused by rearrangement is stronger than the stress decrease part caused by bond-breakings. Nieto et al.[17] and Pan et al.[18] have also observed the phenomenon of multipeaks on the stress−strain curve of GrFs under tension loading, and they have a similar analysis to this paper. According to the stress state at point D in Figure 2b, the areas of stress concentration have no drastic change compared with those at point C, while the holes develop and expand further. In the strain softening stage, the stress in the RLU decreases owing to the new broken bond of cross-links

between G1 and G3. When the shear strain ε equals 1.00, holes further connect and two fracture zones appear in the GrF, and only a few graphene sheets remain connected over the fracture zones, as shown in the black dashed box in Figure 2b.

3.2. The Nonlocalized Fracture. The uniformity of global distribution of broken bonds is quantitatively measured by the coefficient of variation C_v. The calculation method of C_v is shown in Figure 3a, where the model is divided into some
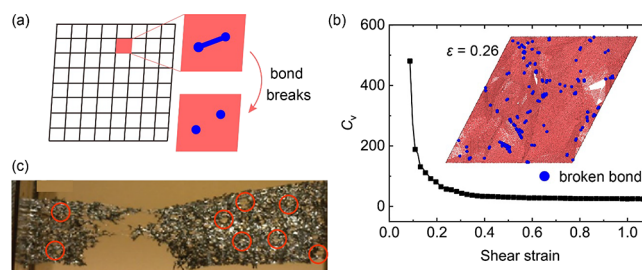

Figure 3. Nonlocalized fracture of GrFs under shear loading. (a) Schematic diagram of calculating the coefficient of variation of bond-breaking distribution C_v. (b) Variation of C_v with shear strain. The inset shows the distribution of bond-breakings when the shear strain is 0.26. Note that the broken bonds are magnified 30 times and projected to the upper surface for visualization. (c) Nonlocalized fracture characteristics in other GrF-based materials. Photograph courtesy of Nieto et al.[43] Copyright 2015 American Chemical Society.

subregions with equal volumes. With the increasing shear strain, the number of broken bonds in each subregion during the loading process is monitored, and then, C_v of broken bonds can be calculated by the ratio of the standard deviation and the average of the number of broken bonds in each subregion. The formula of C_v at every monitoring moment is as follows:

$$C_v = \frac{S_d}{\bar{N}} = \frac{\sqrt{\sum_{i=1}^{n} \frac{(N_i - \bar{N})^2}{n}}}{\bar{N}} \tag{1}$$

where i is the serial number of a certain subregion, n is the total number of subregions, N_i, $\bar{N}$, and S_d are the number of broken bonds in subregion i and the average and standard deviation of broken bonds in all subregions, respectively.

The coefficient of variation is a commonly used statistical parameter to measure the dispersion degree of sets of data. Here, we need to analyze the dispersion degree of broken bonds during the whole loading process, but the total number of broken bonds at each monitoring time is not a constant, so the standard deviation is not applicable to evaluate the evolution of fracture. The coefficient of variation is a dimensionless quantity, calculated by the ratio of standard deviation and average, which can standardize the average of multiple sets of data. Therefore, this parameter is completely applicable to describe the evolution of the distribution of broken bonds in the materials. The method of the coefficient of variation has been widely applied to the characteristic analysis of the statistical distributions of mechanical properties, including ultimate strength or the fatigue limit.[44] The larger the C_v, the more uneven the distribution of broken bonds is, meaning that bond-breakings in GrF are localized. On the contrary, a smaller C_v indicates that the distribution of broken bonds shows the nonlocalized fracture characteristic. The size of subregions should not be too large; otherwise, the statistical data cannot fully demonstrate the concept of "global" or "local" distribution, while it would be much inefficient if the size of

subregions is too small to cover the length of chemical bonds. Thus, the numerical model of GrF is divided into $30 \times 30 \times 30$ subregions ($n = 27{,}000$), each of which contains an average of 7 bonds.

The curve of C_v in the shear loading process is shown in Figure 3b. At the initial time of bond-breakings (shear strain ε is about 0.11), there are two broken bonds in the GrF, and the average and standard deviation of broken bonds in all subregions are 4.32×10^{-6} and 0.0021, respectively, so C_v is 480.86. With the increase in shear strain, the number of broken bonds rises and bond-breakings distribute globally, so C_v decreases rapidly. When the shear strain is about 0.26, there are 164 broken bonds across the GrF, and the average and standard deviation of broken bonds in all subregions are 3.54×10^{-4} and 0.0196, respectively, leading to a relatively small value of C_v of 55.31. When the shear strain gets to 1.00, C_v decreases to 24.74, meaning that the distribution of fracture is almost uniform.

The curve of C_v drops rapidly when the shear strain is 0.11–0.26, which coincides well with the characteristics of the yield stage described in Section 3.1: The GrF enters the yield stage when bond-breakings happen and are gradually distributed globally, causing the rearrangement of geometry and stress across the GrF, which undergoes strain hardening after the cumulative stress increase. The inset of Figure 3b shows the distribution of broken bonds at the beginning of the strain hardening stage ($\varepsilon = 0.26$), in which the particles at both ends of the broken bonds are enlarged and projected onto the upper surface in a blue color for visualization. It can be seen that the positions of bond-breakings are nonlocalized. The fractures in GrFs with different graphene layers are also nonlocalized, as seen from Figure S3 in the Supporting Information.

Analogous nonlocalized fracture has also been confirmed in GrF-based materials. For instance, in a GrF-based hybrid graphene foam/polylactic acid−poly-ε-caprolactone copolymer (Figure 3c), nonlocalized fracture in tensile tests can be observed as shown by the red circles, and the foam underwent necking and finally broke in a ductile manner with an uneven fracture surface.[43]

Gao's team[32] reported in their review about the fracture of graphene that the crack path of a single graphene sheet propagates along the crack tip and forms a fracture zone locally, independent of loading conditions such as chemical, irradiation, quasi-static, and dynamic fracture. Zhang et al.[45] verified the applicability of the classical Griffith brittle fracture theory[46] in the defect-free graphene sheet through experimental observation and theoretical analysis. Different from the localized fracture in regular and ordered single graphene sheets, the 3D graphene assembly shows the nonlocalized fracture characteristic, which is mainly caused by the porous structure of this kind of disordered material. It is easy for the cross-links between the building blocks to become the stress concentration areas and break after reaching the load-bearing limits; then, the degree of freedom of the graphene sheets that once connected increases, accumulated energy is released, and the stress concentration is eliminated. After that, the bond-breakings occur at other chemical bonds, which newly reach the load-bearing limit and are not affected by the bond-breaking events at the previous moments, so the distribution of bond-breakings presents the nonlocalized and gradual evolution.

3.3. The Rearrangement of Geometry and Stress. In order to quantitatively describe the rearrangement of geometry

of graphene sheets, the angle θ between each graphene sheet and the shear direction during the loading process is calculated, and then, the arithmetic average angle $\overline{\theta}$ is obtained. By analyzing the change law of the average angle with shear strain, the trend of the rearrangement of geometry of GrFs can be depicted. The rearrangement of geometry and stress in GrFs is
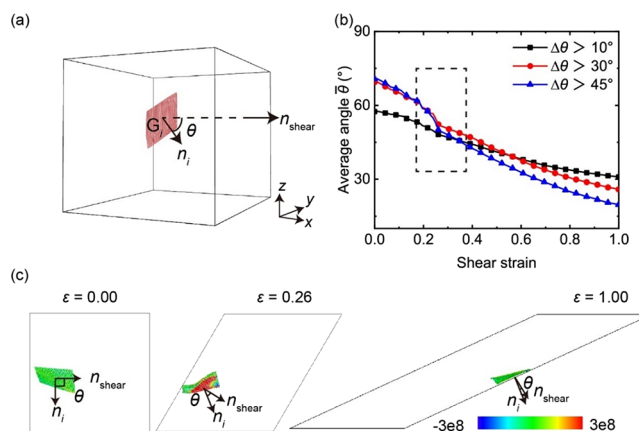

Figure 4. Rearrangement of geometry and stress in GrFs. (a) Schematic diagram of the angle θ between graphene sheets G_i and the loading direction. (b) Variation of the average angle $\overline{\theta}$ with shear strain. (c) Evolution of geometry and stress of a graphene sheet during the shear loading process.

shown in Figure 4. Figure 4a presents the diagram for calculating the average angle, and the formula is as follows:

$$\overline{\theta} = \frac{\sum_{i=1}^{N_G} \theta_i}{N_G} = \frac{\sum_{i=1}^{N_G} \langle n_i, n_{\text{shear}} \rangle}{N_G} \qquad (2)$$

where i is the serial number of graphene sheets (from 1 to 100 in our numerical model), N_G is the total number of graphene sheets in GrF ($N_G = 100$), and n_i and n_{shear} are the normal vectors of the graphene sheet G_i and the shear direction of the current simulation box, respectively. By calculating the angle between n_i and n_{shear} and taking the acute angle into consideration, the inclination angle θ_i of the graphene sheet G_i can be obtained. The average angle $\overline{\theta}$ is the arithmetic angle of the inclination angles of all graphene sheets.

It should be noted that in the 3D structure, not all the graphene sheets will align to the shear direction, and some of the graphene sheets play the role of structural supports, which are called structural graphene sheets. The rotation of these graphene sheets under shear loading is small, that is, the difference of the inclination angle between the initial time and the end time of loading $\Delta\theta$ is very slight. For example, the graphene sheets in 5-layer GrF with $\Delta\theta < 5°$ account for about 24%. Therefore, in order to accurately calculate the average angle of graphene sheets caused by shear loading, the part of structural graphene sheets should be excluded in statistical analysis in a proper way.

The change of the average angle during shear loading is shown in Figure 4b. Without losing generality, the graphene sheets with rotation angles $\Delta\theta > 10$, 30, and 45° were selected for statistical analysis. The proportions of graphene sheets meeting $\Delta\theta > 10$, 30, and 45° are 63, 23, and 14%, respectively. Three curves in Figure 4b decrease monotonically with the increase in shear strain, and all the inflection points is

appear at ε = 0.26. The tangent slope of the curves can reflect the deflection speed of graphene sheets. The slope of the same curve is larger before the inflection point compared to that when ε > 0.26 (the trend for the curve of $\Delta\theta$ > 45° is more obvious than the other two since more structural graphene sheets are eliminated), which indicates that there are drastic rearrangements of geometry in the GrF before the inflection points. Rearrangement of geometry and stress causes the occurrence of the strain hardening stage (0.26 ≤ ε < 0.31).

Take a graphene sheet with a large rotation angle $\Delta\theta$ > 45° for example to present the rearrangement of geometry and stress, as shown in Figure 4c. When the shear strain is 0.00, the graphene sheet is almost perpendicular to the shear direction, and the stress in the sheet is relatively small featured by green contour. When the shear strain increases to 0.26, the graphene sheet has obviously aligned to the shear direction since θ is significantly reduced, and there is high stress concentration in the graphene sheet. When the shear strain gets to 1.00, the normal vector of the graphene sheet almost coincides with the shear direction.

The alignment of graphene sheets along the loading direction was also observed under tensile loading. Nieto et al.[17] carried out *in situ* tensile tests on GrFs and observed that some graphene sheets aligned to the tensile direction, utilizing the in-plane strength advantage of 2D sheets, so the tension modulus was four orders of magnitude higher than that of the compression modulus. Pan et al.[18] reproduced the alignment of the building blocks of GrFs under tensile loading based on CGMD and reported that the rearrangement of graphene sheets is part of the reason for the viscoelasticity of the material.

Under tension and shear loading, the building blocks in GrFs can slip relatively, and the chemical bonds break when they reach the fracture strain. Both tension and shear loading provide the allowable deformation space for the graphene sheets, so the geometry and stress can be rearranged when the degree of freedom is released after bond-breakings. However, there is no alignment and few bonds break in the case of compression, where the strain hardening at a compressive strain of approximately −0.90 is mainly caused by the bending deformation and the sudden increase in van der Waals repulsion.[21]

3.4. The Strain Hardening Mechanism. Figure 5 illustrates the strain hardening regime of GrFs under shear loading. The shear stress, the fraction of broken bonds f_{broken}, the coefficient of variation of bond-breakings C_v, the curve of the average angle $\overline{\theta}$ between graphene sheets ($\Delta\theta$ > 45°), and the shear loading with shear strain ε are plotted in Figure 5a to reflect the mechanism of strain hardening. In the yield stage of the stress−strain curve (0.26 ≤ ε < 0.31), f_{broken} increases rapidly, and accordingly, C_v decreases drastically, reflecting the characteristic of nonlocalized fracture. At the same time, the change rate of $\overline{\theta}$ (the tangent slope of the curve) is relatively higher, meaning strong rearrangement of geometry in GrFs, which is always accompanied by the rearrangement of stress. All of those prove that the strain hardening stage is caused by the nonlocalized fractures and resultant rearrangement of geometry and stress.

The evolution of microstructures is illustrated by the schematic diagram shown in Figure 5b, in which two graphene sheets are connected by a cross-link. Under the external shear loading, the cross-link reaches its load-bearing limit and breaks, and then, two graphene sheets can move freely and align to the
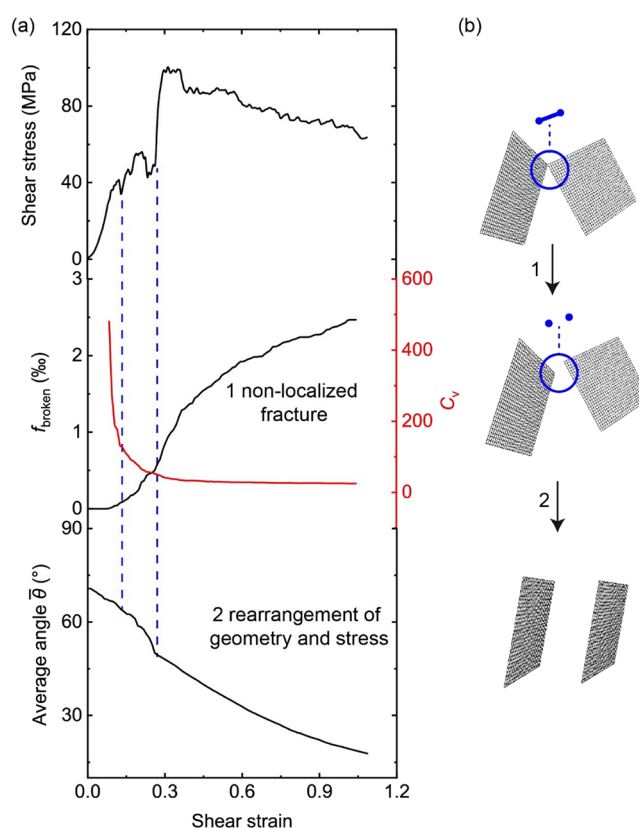

Figure 5. Mechanism of the strain hardening in GrFs. (a) Synchronous variation of shear stress, the fraction of broken bonds, the coefficient of variation of bond-breaking distribution, and the average angle with shear strain. (b) Microstructural diagram of the strain hardening regime.

shear direction, making better use of the high in-plane strength. The cumulative events of these microstructures eventually lead to the strain hardening of GrFs.

Zhou's team[20] studied the mechanical response of GrFs under shear loading using AAMD. It was found that GrFs could promptly form stable structures under shear deformation and remain their stability during subsequent annealing treatment. Thus, they suggested that the internal configuration of GrFs can be tuned by shear loading and the structure can be stabilized after the rearrangement. In addition, the strain hardening regime of GrFs under shear loading was also revealed by Xia et al.[19] through CGMD. This paper further revealed the mechanism of strain hardening, which enriches the understanding of the 3D graphene assembly.

The strain hardening regime is also widely observed in metals and polymer materials. Taking steel as an example, its internal microstructures change after plastic deformation.[47] The grains are elongated along the direction of maximum deformation, and the lattice is distorted; thus, the resistance to deformation is improved. For polymers, the strain hardening behavior is mainly caused by the alignment of the chain network, which is initially entangled along the tension direction.[23] There have been mature preparation processes to take advantage of this strain hardening regime for improving the mechanical performance of these materials. During the manufacturing process of metals, strength can be improved after realizing strain hardening by increasing dislocation density, adding a second phase to make an alloy, or changing the distribution of the grain size.[22] For the same reason, we can
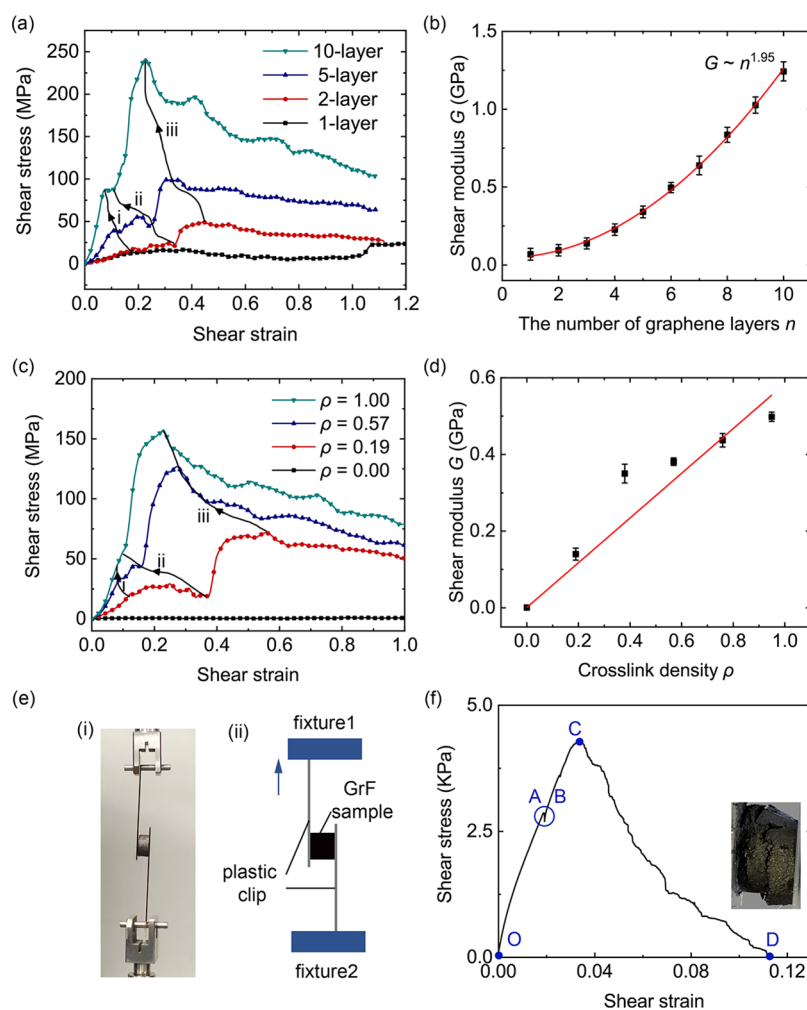
Figure 6. Effect of the number of graphene layers and cross-link density on mechanical properties of GrFs under shear loading. (a) Stress−strain curves of GrFs with different layers of graphene. (b) Relationship between shear modulus G and the number of graphene layers n. (c) Stress−strain curves of GrFs with different cross-link densities. (d) Relationship between shear modulus G and cross-link density ρ. (e) Shear test of GrFs. (i) Loading device. (ii) Schematic diagram of shear loading. (f) Stress−strain curve of GrF under shear loading in experiments. The inset shows the fracture of the GrF sample.

tune the mechanical responses of GrFs effectively based on the unveiled mechanism of strain hardening in Figure 5.

3.5. The Effects of the Number of Graphene Layers and Cross-Link Density. Figure 6 shows the mechanical response of GrFs with different graphene layers or cross-link densities under shear loading. GrFs assembled from 1, 2, 5, and 10 layers of graphene sheets with the same relative cross-link density of 0.47 are obtained, and their stress−strain curves are shown in Figure 6a. The results of other graphene layers can be found in Figure S4 in the Supporting Information. GrFs with different graphene layers undergo the same stages, including the linear elastic, yield plateau, strain hardening, and post-peak strain softening stages. Shear stiffness and shear strength are the slope of the linear elastic stage and the peak value of the stress−strain curve, respectively.

With the increase in the number of graphene layers n, (1) the shear modulus G increases, satisfying a power scaling law of $G \sim n^{1.95}$ (Figure 6b); (2) the initiation strain of the yielding stage decreases indicated by the arrow i since the initial bond-breaking happens earlier, as bonds reach the loading limit faster in the harder GrFs than in the softer GrFs (see more details in Figure S4); (3) the yielding stage is shortened, and the initiation strain of the strain hardening stage is smaller

indicated by the arrow ii; in structures composed of more graphene layers, stress adjusts and increases more rapidly after bond-breakings, leading to a prompt offset of the stress reduction caused by broken bonds, and the overall stress increase becomes the dominant pattern in harder GrFs earlier than in the softer GrFs; (4) the peak strain decreases, and the shear strength increases indicated by the arrow iii.

GrFs assembled from 5-layer graphene sheets connected by different cross-link densities are obtained to analyze the effect of cross-link density ρ on the mechanical response of the material under shear loading, as shown in Figure 6c. When ρ equals 0.00, 0.19, and 0.57, the general trends of stress−strain curves are similar, including the linear elastic, yield, strain hardening, and strain softening stages, identical with the main stress stages in Figure 6a. However, for the structure with a large number of cross-links ($\rho = 1.00$), the yield plateau is obscure because the rapid massive bond-breakings cause the drastic rearrangement of geometry and stress, leading to the material entering the strain hardening stage rapidly right after the linear elastic stage.

With the increase in cross-link density, (1) the shear modulus increases in a linear fashion because of the good stress transfer capability (Figure 6d); (2) the initiation strain in the

yielding stage decreases indicated by the arrow i since the initial bond-breaking happens earlier (see more details in Figure S5); (3) the yielding stage is shortened, and the initiation strain of the strain hardening stage decreases indicated by the arrow ii since the stress increase soon becomes the dominant part owing to the good connectivity and wide load-bearing paths; (4) the peak point occurs earlier, and the shear strength increases as indicated by the arrow iii.

As shown in Figure 6e-i, shear tests were carried out using commercial GrFs prepared by an assembly method with the disorderly porous structure shown in Figure 1c. More details about the experimental samples are given in the part of "Experimental Information" at the end of this paper. The shear loading is applied by a deformation-controlled method by moving the fixture1 up while keeping the fixture2 still (Figure 6e-ii). The stress−strain curve (Figure 6f) is consistent qualitatively with the result of the GrF with $\rho = 1.00$ in Figure 6c, including the linear elastic stage OA, yield point AB, strain hardening BC, and the failure period CD (the failure state of the GrF is shown in the inset of Figure 6f), which is due to the high cross-link density in experimental samples.

In addition to the above-mentioned configuration parameters, the strain hardening regime is also independent of the ambient temperature, as shown in Figure S5. This temperature-invariant characteristic is in good agreement with the thermal stability observed in carbon-based materials such as carbon nanotubes[48] and GrFs,[2] which can maintain good elasticity even in extreme conditions (from −196 to 1000 °C), while other polymer materials such as rubbers possess a limited operational temperature range (for example, for silicone rubber, it is −55 to 300 °C).[48]

These analyses are particularly useful to provide inspiration for better applications. For instance, the anode materials in lithium-ion batteries often adopt the porous GrF as a structural skeleton, in which Si nanospheres are embedded to resist volume variations during charging and discharging.[6] In this sense, the mechanical properties of the GrF chiefly determine the durability and tolerable working conditions of the batteries, which could be enhanced by utilizing the strain hardening regime. Moreover, in many GrF-based devices used for gas detection and sorbents, one of the most basic requirements is the mechanical robustness of the GrF.[5,49] The bearing capacity and connectivity are expected to be optimized considering the strain hardening behavior. Particularly, the fracture and failure of materials are crucial issues in applications such as stretchable electronic devices and biocompatible scaffolds,[43,50] so the nonlocalized fracture of GrF and the resultant local failures of the material must be determined. As graphene is an excellent pioneer of 2D materials, these related studies can provide a meaningful understanding of the design and applications of booming 2D materials and their 3D assemblies.[51]

4. CONCLUSIONS

The structural and mechanical properties of GrFs under shear loading are systematically investigated using CGMD. Different from the continuous solid materials like metals, the bond-breakings in GrFs are global, and the fracture propagation is nonlocalized rather than growing along a local crack tip, ensued by the rearrangement of geometry and stress of graphene sheets. The cumulative events of nonlocalized fracture and resultant rearrangement of geometry and stress lead to the strain hardening regime after the yield plateau. The strain hardening phenomenon exists widely in GrFs with

various configuration parameters such as the number of graphene layers and the cross-link densities. The shear stiffness increases in a linear manner with cross-link density and satisfies the power law $G \sim n^{1.95}$ with the number of graphene layers but independent of the ambient temperature. These results could not only provide a valuable understanding of the graphene assembly to further optimize its design and engineering applications but also inspire the apprehension of other appealing 3D porous assemblies based on 2D materials.

5. EXPERIMENTAL INFORMATION

The experiment shown in Figure 6e,f was done using the Instron 5848 MicroTester. GrF samples were purchased from Best Materials Co., Ltd. (http://www.jiacaikeji1899.com). By using a self-assembly method, the graphene oxide foams were first prepared on the basis of graphene oxide, and then, a reduction procedure under high temperature was applied to obtain porous GrFs. The purity was greater than 99%. The samples used in the experiment were cylinders with a height of 10 ± 2 mm and a diameter of 20 ± 2 mm.

■ ASSOCIATED CONTENT

Ⓢ Supporting Information

The Supporting Information is available free of charge at https://pubs.acs.org/doi/10.1021/acsomega.1c03127.

Parameters of the force field, supplementary mechanical behaviors, and further discussions (PDF)

■ AUTHOR INFORMATION

Corresponding Authors

Chao Wang − *LNM, Institute of Mechanics, Chinese Academy of Sciences, Beijing 100190, China; School of Engineering Science, University of Chinese Academy of Sciences, Beijing 100049, China;* ⓞ orcid.org/0000-0002-3234-6917; Phone: 010 8254 3525; Email: wangchao@lnm.imech.ac.cn

Zuobing Wu − *LNM, Institute of Mechanics, Chinese Academy of Sciences, Beijing 100190, China; School of Engineering Science, University of Chinese Academy of Sciences, Beijing 100049, China;* Phone: 010 8254 3955; Email: wuzb@lnm.imech.ac.cn

Author

Tian Yang − *LNM, Institute of Mechanics, Chinese Academy of Sciences, Beijing 100190, China; School of Engineering Science, University of Chinese Academy of Sciences, Beijing 100049, China*

Complete contact information is available at:
https://pubs.acs.org/10.1021/acsomega.1c03127

Author Contributions

C.W. conceived the original idea and designed and supervised the simulations. T.Y. formulated the numerical model, conducted all the simulations, and drafted the paper. All authors reviewed the manuscript.

Notes

The authors declare no competing financial interest.

■ ACKNOWLEDGMENTS

■ REFERENCES

(1) Xu, X.; Zhang, Q.; Yu, Y.; Chen, W.; Hu, H.; Li, H. Naturally dried graphene aerogels with superelasticity and tunable Poisson's ratio. *Adv. Mater.* **2016**, *28*, 9223−9230.

(2) Wu, Y.; Yi, N.; Huang, L.; Zhang, T.; Fang, S.; Chang, H.; Li, N.; Oh, J.; Lee, J. A.; Kozlov, M.; Chipara, A. C.; Terrones, H.; Xiao, P.; Long, G.; Huang, Y.; Zhang, F.; Zhang, L.; Lepró, X.; Haines, C.; Lima, M. D.; Lopez, N. P.; Rajukumar, L. P.; Elias, A. L.; Feng, S.; Kim, S. J.; Narayanan, N. T.; Ajayan, P. M.; Terrones, M.; Aliev, A.; Chu, P.; Zhang, Z.; Baughman, R. H.; Chen, Y. Three-dimensionally bonded spongy graphene material with super compressive elasticity and near-zero Poisson's ratio. *Nat. Commun.* **2015**, *6*, 6141.

(3) Qiu, L.; Huang, B.; He, Z.; Wang, Y.; Tian, Z.; Liu, J. Z.; Wang, K.; Song, J.; Gengenbach, T. R.; Li, D. Extremely low density and super-compressible graphene cellular materials. *Adv. Mater.* **2017**, *29*, 1701553.

(4) Worsley, M. A.; Pauzauskie, P. J.; Olson, T. Y.; Biener, J.; Satcher, J. H., Jr.; Baumann, T. F. Synthesis of graphene aerogel with high electrical conductivity. *J. Am. Chem. Soc.* **2010**, *132*, 14067−14069.

(5) Bi, H.; Xie, X.; Yin, K.; Zhou, Y.; Wan, S.; He, L.; Xu, F.; Banhart, F.; Sun, L.; Ruoff, R. S. Spongy graphene as a highly efficient and recyclable sorbent for oils and organic solvents. *Adv. Funct. Mater.* **2012**, *22*, 4421−4425.

(6) Chen, S.; Bao, P.; Huang, X.; Sun, B.; Wang, G. Hierarchical 3D mesoporous silicon@graphene nanoarchitectures for lithium ion batteries with superior performance. *Nano Res.* **2013**, *7*, 85−94.

(7) Ma, Y.; Chang, H.; Zhang, M.; Chen, Y. Graphene-based materials for lithium-ion hybrid supercapacitors. *Adv. Mater.* **2015**, *27*, 5296−5308.

(8) Bi, H.; Xie, X.; Yin, K.; Zhou, Y.; Wan, S.; Ruoff, R. S.; Sun, L. Highly enhanced performance of spongy graphene as an oil sorbent. *J. Mater. Chem. A* **2014**, *2*, 1652−1656.

(9) Xu, X.; Guan, C.; Xu, L.; Tan, Y. H.; Zhang, D.; Wang, Y.; Zhang, H.; Blackwood, D. J.; Wang, J.; Li, M.; Ding, J. Three dimensionally free-formable graphene foam with designed structures for energy and environmental applications. *ACS Nano* **2019**, *14*, 937−947.

(10) Li, J.; Zhao, S.; Zeng, X.; Huang, W.; Gong, Z.; Zhang, G.; Sun, R.; Wong, C. P. Highly stretchable and sensitive strain sensor based on facilely prepared three-dimensional graphene foam composite. *ACS Appl. Mater. Interfaces* **2016**, *8*, 18954−18961.

(11) Idowu, A.; Boesl, B.; Agarwal, A. 3D graphene foam-reinforced polymer composites - a review. *Carbon* **2018**, *135*, 52−71.

(12) Yang, M.; Zhao, N.; Cui, Y.; Gao, W.; Zhao, Q.; Gao, C.; Bai, H.; Xie, T. Biomimetic architectured graphene aerogel with exceptional strength and resilience. *ACS Nano* **2017**, *11*, 6817−6824.

(13) Pan, D.; Wang, C.; Wang, X. Graphene foam: hole-flake network for uniaxial supercompression and recovery behavior. *ACS Nano* **2018**, *12*, 11491−11502.

(14) Wang, C.; Zhang, C.; Chen, S. Micro-mechanism and influencing factors of graphene foam elasticity. *Carbon* **2019**, *148*, 267−276.

(15) Qin, Z.; Jung, G. S.; Kang, M. J.; Buehler, M. J. The mechanics and design of a lightweight three-dimensional graphene assembly. *Sci. Adv.* **2017**, *3*, 1601536.

(16) Patil, S. P.; Shendye, P.; Markert, B. Molecular investigation of mechanical properties and fracture behavior of graphene aerogel. *J. Phys. Chem. B* **2020**, *124*, 6132−6139.

(17) Nieto, A.; Boesl, B.; Agarwal, A. Multi-scale intrinsic deformation mechanisms of 3D graphene foam. *Carbon* **2015**, *85*, 299−308.

(18) Pan, D.; Wang, C.; Wang, T. C.; Yao, Y. Graphene foam: uniaxial tension behavior and fracture mode based on a mesoscopic model. *ACS Nano* **2017**, *11*, 8988−8997.

(19) Xia, W.; Vargas-Lara, F.; Keten, S.; Douglas, J. F. Structure and dynamics of a graphene melt. *ACS Nano* **2018**, *12*, 5427−5435.

(20) Baimova, J. A.; Rysaeva, L. K.; Liu, B.; Dmitriev, S. V.; Zhou, K. From flat graphene to bulk carbon nanostructures. *Phys. Status Solidi B* **2015**, *252*, 1502−1507.

(21) Wang, C.; Zhang, C.; Chen, S. The microscopic deformation mechanism of 3D graphene foam materials under uniaxial compression. *Carbon* **2016**, *109*, 666−672.

(22) Cahn, R.; Haasen, P.; Kramer, E.; Mughrabi, H. *Plastic deformation and fracture of materials*; VCH, 1993.

(23) Ward, I.; Klein, P. *Polymer Physics*; John Wiley & Sons, Ltd, 2007.

(24) Zhang, X.; Zhong, L.; Mateos, A.; Kudo, A.; Vyatskikh, A.; Gao, H.; Greer, J. R.; Li, X. Theoretical strength and rubber-like behaviour in micro-sized pyrolytic carbon. *Nat. Nanotechnol.* **2019**, *14*, 762−769.

(25) Patil, S. P.; Kulkarni, A.; Markert, B. Shockwave response of graphene aerogels: an all-atom simulation study. *Comput. Mater. Sci.* **2021**, *189*, 110252.

(26) Cranford, S.; Buehler, M. J. Twisted and coiled ultralong multilayer graphene ribbons. *Modell. Simul. Mater. Sci. Eng.* **2011**, *19*, No. 054003.

(27) Coleman, J. N.; Lotya, M.; O'Neill, A.; Bergin, S. D.; King, P. J.; Khan, U.; Young, K.; Gaucher, A.; De, S.; Smith, R. J.; Shvets, I. V.; Arora, S. K.; Stanton, G.; Kim, H.-Y.; Lee, K.; Kim, G. T.; Duesberg, G. S.; Hallam, T.; Boland, J. J.; Wang, J. J.; Donegan, J. F.; Grunlan, J. C.; Moriarty, G.; Shmeliov, A.; Nicholls, R. J.; Perkins, J. M.; Grieveson, E. M.; Theuwissen, K.; McComb, D. W.; Nellist, P. D.; Nicolosi, V. Two-dimensional nanosheets produced by liquid exfoliation of layered materials. *Science* **2011**, *331*, 568−571.

(28) Novoselov, K. S.; Jiang, D.; Schedin, F.; Booth, T. J.; Khotkevich, V. V.; Morozov, S. V.; Geim, A. K. Two-dimensional atomic crystals. *Proc. Natl. Acad. Sci. U. S. A.* **2005**, *102*, 10451−10453.

(29) Ruiz, L.; Xia, W.; Meng, Z.; Keten, S. A coarse-grained model for the mechanical behavior of multi-layer graphene. *Carbon* **2015**, *82*, 103−115.

(30) Deng, W.; Fang, Q.; Zhou, X.; Cao, H.; Liu, Z. Hydrothermal self-assembly of graphene foams with controllable pore size. *RSC Adv.* **2016**, *6*, 20843−20849.

(31) Zhang, Y. Y.; Gu, Y. T. Mechanical properties of graphene: effects of layer number, temperature and isotope. *Comput. Mater. Sci.* **2013**, *71*, 197−200.

(32) Zhang, T.; Li, X.; Gao, H. Fracture of graphene: a review. *Int. J. Fract.* **2015**, *196*, 1−31.

(33) Fang, Q.; Shen, Y.; Chen, B. Synthesis, decoration and properties of three-dimensional graphene-based macrostructures: a review. *Chem. Eng. J.* **2015**, *264*, 753−771.

(34) Liang, J.; Zhao, Z.; Tang, Y.; Hao, X.; Wang, X.; Qiu, J. Covalent bonds-integrated graphene foam with superb electro-mechanical properties as elastic conductor and compressive sensor. *Carbon* **2019**, *147*, 206−213.

(35) Nautiyal, P.; Boesl, B.; Agarwal, A. Harnessing three dimensional anatomy of graphene foam to induce superior damping in hierarchical polyimide nanostructures. *Small* **2017**, *13*, 1603473.

(36) Li, Z.; Liu, Z.; Sun, H.; Gao, C. Superstructured assembly of nanocarbons: fullerenes, nanotubes, and graphene. *Chem. Rev.* **2015**, *115*, 7046−7117.

(37) Tao, Y.; Xie, X.; Lv, W.; Tang, D. M.; Kong, D.; Huang, Z.; Nishihara, H.; Ishii, T.; Li, B.; Golberg, D.; Kang, F.; Kyotani, T.; Yang, Q. H. Towards ultrahigh volumetric capacitance: graphene derived highly dense but porous carbons for supercapacitors. *Sci. Rep.* **2013**, *3*, 2975.

(38) Swenson, R. J. Comments on virial theorems for bounded systems. *Am. J. Phys.* **1983**, *51*, 940−942.

(39) Plimpton, S. Fast parallel algorithms for short−range molecular dynamics. *J. Comput. Phys.* **1995**, *117*, 1−19.

(40) Stukowski, A. Visualization and analysis of atomistic simulation data with OVITO—the Open Visualization Tool. *Modell. Simul. Mater. Sci. Eng.* **2010**, *18*, No. 015012.

(41) Cates, M. E.; Wittmer, J. P.; Bouchaud, J.-P.; Claudin, P. Jamming, force chains, and fragile matter. *Phys. Rev. Lett.* **1998**, *81*, 1841−1844.

(42) Ma, Y.; Chen, Y. Three-dimensional graphene networks: synthesis, properties and applications. *Natl. Sci. Rev.* **2015**, *2*, 40−53.

(43) Nieto, A.; Dua, R.; Zhang, C.; Boesl, B.; Ramaswamy, S.; Agarwal, A. Three dimensional graphene foam/polymer hybrid as a high strength biocompatible scaffold. *Adv. Funct. Mater.* **2015**, *25*, 3916−3924.

(44) He, X.; Oyadiji, S. O. Application of coeffcient of variation in reliability-based mechanical design and manufacture. *J. Mater. Process. Technol.* **2001**, *119*, 374−378.

(45) Zhang, P.; Ma, L.; Fan, F.; Zeng, Z.; Peng, C.; Loya, P. E.; Liu, Z.; Gong, Y.; Zhang, J.; Zhang, X.; Ajayan, P. M.; Zhu, T.; Lou, J. Fracture toughness of graphene. *Nat. Commun.* **2014**, *5*, 3782−3786.

(46) Griffith, A. A. The phenomena of rupture and flow in solids. *Philos. Trans. R. Soc., A* **1920**, *A221*, 163−198.

(47) Abbaschian, R.; Abbaschian, L.; Reed-Hill, R. E. *Physical metallurgy principles;* Cengage Learning: Stamford, 2009, *4*.

(48) Xu, M.; Futaba, D. N.; Yamada, T.; Yumura, M.; Hata, K. Carbon nanotubes with temperature-invariant viscoelasticity from −196 °C to 1000 °C. *Science* **2010**, *330*, 1364−1368.

(49) Yavari, F.; Chen, Z.; Thomas, A. V.; Ren, W.; Cheng, H. M.; Koratkar, N. High sensitivity gas detection using a macroscopic three-dimensional graphene foam network. *Sci. Rep.* **2011**, *1*, 166.

(50) Chen, Z.; Ren, W.; Gao, L.; Liu, B.; Pei, S.; Cheng, H. M. Three-dimensional flexible and conductive interconnected graphene networks grown by chemical vapour deposition. *Nat. Mater.* **2011**, *10*, 424−428.

(51) Butler, S. Z.; Hollen, S. M.; Cao, L.; Cui, Y.; Gupta, J. A.; Gutierrez, H. R.; Heinz, T. F.; Hong, S. S.; Huang, J.; Ismach, A. F.; Johnston-Halperin, E.; Kuno, M.; Plashnitsa, V. V.; Robinson, R. D.; Ruoff, R. S.; Salahuddin, S.; Shan, J.; Shi, L.; Spencer, M. G.; Terrones, M.; Windl, W.; Goldberger, J. E. Progress, challenges, and opportunities in two-dimensional materials beyond graphene. *ACS Nano* **2013**, *7*, 2898−2926.